coatings

Article

# Chemical Solution Deposition of YBCO Films with Gd Excess

**Valentina Pinto** [1], **Angelo Vannozzi** [1], **Achille Angrisani Armenio** [1], **Francesco Rizzo** [1], **Andrea Masi** [2], **Antonino Santoni** [3], **Alexander Meledin** [4,5], **Fabrizio Mario Ferrarese** [1], **Silvia Orlanducci** [6] and **Giuseppe Celentano** [1,*]

[1] Superconductivity Section, FSN-COND, ENEA, Via Enrico Fermi 45, Frascati, 00044 Rome, Italy; valentina.pinto@enea.it (V.P.); angelo.vannozzi@enea.it (A.V.); achille.angrisaniarmenio@enea.it (A.A.A.); francesco.rizzo@enea.it (F.R.); fabrizio.ferrarese92@gmail.com (F.M.F.)
[2] Engineering Department, Roma Tre University, Via Vito Volterra 62, 00146 Rome, Italy; andrea.masi@uniroma3.it
[3] FSN-TECFIS-MNF, ENEA, v. E. Fermi 45, Frascati, 00044 Rome, Italy; antonino.santoni@enea.it
[4] Central Facility for Electron Microscopy, RWTH Aachen University, 52074 Aachen, Germany; meledin@gfe.rwth-aachen.de
[5] Ernst Ruska-Centre for Microscopy and Spectroscopy with Electrons (ER-C), Forschungszentrum Jülich GmbH, 52428 Jülich, Germany
[6] Department of Chemical Sciences and Technologies, Tor Vergata University, Via della Ricerca Scientifica, 00133 Rome, Italy; silvia.orlanducci@uniroma2.it
* Correspondence: giuseppe.celentano@enea.it

Received: 5 August 2020; Accepted: 2 September 2020; Published: 4 September 2020

**Abstract:** Chemical solution deposition of Gd-doped YBCO, $Y_1Gd_yBa_2Cu_3O_{7-\delta}$, (YBCO-Gd), film was carried out following the metal-organic decomposition approach and *in situ* route. Two dopant concentrations, 5 and 10 mol %, were evaluated. The morphology and crystalline structure of the superconductor films were deeply investigated. In general, a homogeneous and well *c*-axis oriented film was observed by using scanning and transmission electron microscopy (SEM and TEM) and X-ray diffraction. However, compared to pure YBCO, YBCO-Gd samples showed an increased stacking faults concentration, as recognized by TEM. X-ray photoelectron spectroscopy allowed studying the Gd distribution in the films and gathered information about the Gd electronic environment. Superconducting properties were evaluated at different temperatures, magnetic field directions, and intensities. Higher zero-field critical current densities were measured with respect to undoped samples in the temperature range from 10 to 77 K with both Gd concentrations (i.e., 28, 27, and 13 MA·cm$^{-2}$, respectively, for YBCO-Gd 5%, YBCO-Gd 10%, and undoped YBCO at 10 K in self field condition). At low temperatures, this improvement was maintained up to 12 T, confirming the efficacy of Gd addition for the enhancement of transport properties of YBCO film.

**Keywords:** $YBa_2Cu_3O_{7-\delta}$ (YBCO); $GdBa_2Cu_3O_{7-\delta}$ (GdBCO); $YGd_yBa_2Cu_3O_{7-\delta}$; chemical solution deposition (CSD); metal-organic decomposition (MOD); *in situ* approach; low-fluorine route; artificial pinning center (APC)

## 1. Introduction

Several studies have been carried out on the substitution of $Y^{3+}$ in $YBa_2Cu_3O_{7-\delta}$ (YBCO) by rare earth elements (RE), such as $Er^{3+}$, $Ho^{3+}$, and $Gd^{3+}$, to form $REBa_2Cu_3O_{7-\delta}$ (REBCO) compounds. Their superconducting properties are generally improved with respect to YBCO due to the higher critical temperature ($T_c$) values and, consequently, higher irreversibility fields ($H_{irr}$) at 77 K [1]. Among REBCO systems, $GdBa_2Cu_3O_{7-\delta}$ (GdBCO) is one of the most investigated and extensively adopted for coating conductors manufacturing. GdBCO thin films can be successfully deposited through physical [2–4] and chemical methods [5,6], being the latter ones less expensive and, consequently, more appealing from an industrial point of view [7], which is a key issue in the perspective of application technology development. However, with respect to pure YBCO, chemical solution deposition (CSD) of GdBCO film requires more accurate control of the process parameters, especially during the crystallization step. In fact, GdBCO nucleation is favored by higher growth temperatures, faster ramp rates, and lower oxygen partial pressure ($pO_2$) than those used in the YBCO process [8–11].

Driven by the works on YBCO films, a great number of studies have been carried out on GdBCO doping with oxides, such as $BaZrO_3$, $BaHfO_3$, $Gd_2O_3$, aimed at introducing artificial pinning centers (APCs) to improve film performances when an external magnetic field is applied [5,6,10,12]. On the other hand, mixed compounds, such as $Y_{1-x}Gd_xBa_2Cu_3O_{7-\delta}$ ($0 < x < 1$), have been proposed and studied as a suitable alternative route for the improvement of vortex pinning capabilities [13–18].

To our knowledge, the addition of Gd in stoichiometric excess with respect to Y, $Y_1Gd_yBa_2Cu_3O_{7-\delta}$, has been reported only by two papers: Xu et al. [19] studied the $Gd_2O_3$ introduction in YBCO bulk, and Li et al. [20] grew, through a sol-gel process, YBCO films doped with Gd 10 and 50 mol %. These articles have shown promising results with enhanced critical current density ($J_c$) in both self-field and in-field conditions at 65 and 77 K, respectively. Therefore, in the present paper, we proposed a similar study applied to Gd doped YBCO film (YBCO-Gd) deposited by CSD and a low-fluorine metal-organic decomposition (MOD) approach. The low-fluorine formulation has already demonstrated to be suitable for GdBCO deposition, even better than the solution composed by all trifluoroacetate precursors, the so-called TFA-route [5,21]. Our work aimed at exploring whether effective defects could be introduced in YBCO film through the *in situ* low-fluorine MOD technique, i.e., using a single solution with YBCO and Gd precursor salts, and at determining the temperature and magnetic field regimes in which their contribution is more favorable. The introduction of zero-dimensional defects by CSD is generally carried out by the *ex-situ* route, based on the addition of preformed nanoparticles to the YBCO metal-organic precursor solution [22,23]. On the contrary, the *in situ* process has demonstrated to have limited control over the particle size of secondary phases that spontaneously segregate during YBCO film growth. Therefore, this system is normally employed for three-dimensional defects generation [24].

However, when added in excess with respect to Y, Gd can play two different roles: it can replace Y to form GdBCO with the exceeding Y, possibly forming other oxides, such as $Y_2O_3$. Otherwise, Gd can form oxides as $Gd_2O_3$. Both situations should contribute to the generation of a complex defects landscape, namely, the formation of several oxides and enhancement of the lattice strain due to the accommodation of two comparable but not identical crystalline cells (i.e., YBCO and GdBCO) [25–27] (Table 1). These nanometric defects, various for chemical nature and size, can act in a synergetic way, determining an overall improvement of the superconducting transport properties [17,28].

**Table 1.** Lattice parameters in orthorhombic REBCO [1] and cubic C-type $RE_2O_3$ [2] phase. RE = Y, Gd.

| Lattice Parameter | YBCO | GdBCO | $Y_2O_3$ | $Gd_2O_3$ |
|---|---|---|---|---|
| $a$ (Å) | 3.8230 (5) | 3.8416 (4) | 10.6021 | 10.8122 |
| $b$ (Å) | 3.8857 (5) | 3.8984 (4) | - | - |
| $c$ (Å) | 11.680 (2) | 11.707 (1) | - | - |
| $V$ (Å$^3$) | 173.5 | 175.32 | 1192 | 1264 |

[1] Rietveld refinements done by [25]. [2] Data from [26,27].

YBCO-Gd films were prepared through the low-fluorine MOD approach and in situ route with two dopant concentrations, 5 and 10 mol %, of Gd with respect to Y. Experiments were carried out using the thermal treatment optimized for YBCO. The purpose was to investigate the fate of Gd when process conditions are unfavorable to GdBCO growth, i.e., high $pO_2$ and slow ramp rate [8,10]. The morphology and crystalline structure of superconductor films were deeply investigated. In general, a homogeneous and well $c$-axis oriented film was observed by using scanning and transmission electron microscopy

(SEM and TEM) and X-ray diffraction (XRD). X-ray photoelectron spectroscopy (XPS) allowed studying the Gd distribution in the films and gather information about the Gd electronic environment.

Results suggested that we could maintain the advantages related to the presence of Gd despite the non-optimum experimental growth conditions. Gd was finely and uniformly dispersed within the YBCO film matrix, likely forming GdBCO. The formation of a large number of stacking faults was also reported. The improved $J_c(H)$ performances of YBCO-Gd films indicated that the rich defect landscape recognized in these samples could act as vortex pinning centers, particularly effective at low-temperature regimes.

## 2. Materials and Methods

YBCO and YBCO-Gd films were deposited following the low-fluorine MOD approach. The YBCO precursor solution was prepared by dissolving in propionic acid (Sigma Aldrich, St. Louis, MO, USA, 99.5%) stoichiometric amounts of yttrium (III) acetate hydrate (Sigma Aldrich, 99.9%), barium (II) trifluoroacetate hydrate (Alfa Aesar, Haverhill, MA, United States), and copper (II) acetate (Alfa Aesar 99.9%). The Y:Ba:Cu ratio was equal to 1:2:3, and the final solution concentration corresponded to [YBCO] = 0.2 M. Further details on the solution preparation can be found elsewhere [29]. YBCO-Gd solutions were prepared through the *in situ* approach, using a single solution with YBCO and Gd precursor salts and comparing two dopant concentrations, 5 and 10 mol %, of Gd (added as gadolinium (III) acetate hydrate, Sigma Aldrich, 99.9%) with respect to Y. Precursor solutions were spin-coated for 60 s at a spinning rate of 3000 rpm on (001) strontium titanate, $SrTiO_3$ (STO), single crystals (supplied by Wollemi).

Films were pyrolyzed in a quartz tube furnace with flowing oxygen (0.94 L $min^{-1}$, humid for $T > 100$ °C) up to 480 °C using the following heating ramp rate: 10 °C $min^{-1}$ (up to 90 °C), 2.5 °C $min^{-1}$ (in the range 90–200 °C), 1.2 °C $min^{-1}$ (in the range 200–300 °C), 10 °C $min^{-1}$ (in the range 300–480 °C), 10 °C $min^{-1}$ (during the cooling step). A second treatment, named "Firing", was then performed to promote YBCO crystallization and oxygenation: firstly, the sample was heated with a rate of 10 °C·$min^{-1}$ to the dwell temperature of 830 °C, kept for 50 min in a humid mixture of nitrogen and oxygen (flow rate $N_2$: 2.83 L $min^{-1}$, $O_2$: $1.15 \cdot 10^{-3}$ L $min^{-1}$) and further 10 min in the same dry mixture (crystallization step). Subsequently, the film was cooled down to 450 °C with a rate of 10 °C·$min^{-1}$, kept at this temperature for 15 min in dry oxygen (0.94 L·$min^{-1}$) for the oxygenation step and then cooled to room temperature with the same ramp rate. The aforementioned procedure was defined as the "standard" process. Several experiments were carried out varying some parameters of the thermal treatment in order to estimate if the YBCO-Gd system needs, as $Y_{1-x}Gd_xBa_2Cu_3O_{7-\delta}$, $0 < x \leq 1$, compounds, a precise optimization of the processing conditions. In particular, a faster heating/cooling ramp rate of 30 °C $min^{-1}$ (fast process) was studied in comparison with the standard process (10 °C $min^{-1}$). A sample of pure YBCO film, used as a reference, was always deposited together with YBCO-Gd films. A final thickness of 75 nm was obtained for both YBCO and YBCO-Gd films. Structural characterizations were carried out employing XRD. The θ-2θ and ω-scans were performed by a Rigaku Geigerflex diffractometer with Cu Kα radiation in Bragg Brentano configuration. Film morphology was evaluated by SEM images, obtained using a Gemini LEO 1525 field emission high-resolution SEM with 20 kV operating voltage and in-lens high-resolution annular detector. XPS data were acquired in an ultra-high vacuum system operating at $2 \times 10^{-8}$ Pa base pressure and equipped with a CLAM2 hemispherical analyzer working at constant pass energy mode and calibrated on the Ag $3d_{5/2}$ and Ag M4NN lines according to [30] and by setting at 285 eV the binding energy (BE) of the adventitious carbon C1s core-level measured on the as-inserted sample. For quantification, data were normalized to the photoelectron cross-section, analyzer transmission function, and electron mean free path. The estimated BE maximum error was ±0.1 eV. $Ar^+$ etching was used for depth profiling. For sample etching, a PSP Vacuum Technology ISIS 3000 system was used as the $Ar^+$ ion source. The samples were bombarded with a defocused beam of 1000 eV $Ar^+$ ions at about 18 μA total sample current. The sputtering rate was calibrated against a sample of a known thickness. The YBCO-Gd sample was inserted into the analysis chamber "as received”. The $Gd_2O_3$ sample (PLD target, 99.95% supplied by Franco Corradi) used for reference was prepared in a glove box in the $N_2$ atmosphere and then loaded into the XPS sample load-lock system without exposure to the atmosphere.

For TEM investigations, a cross-sectional lamella was produced by a focused ion beam (FIB) technique, employing an FEI Dual Beam Helios NanoLab system (FEI, Thermo Fisher, OR, USA). The annular dark-field and high-angle annular dark-field scanning transmission electron microscopy (ADF and HAADF-STEM) imaging and energy-dispersive X-ray spectroscopy (EDX) were performed using an FEI Titan electron microscope, equipped with a Cs-aberration corrector for the probe-forming lens and a “Super-X” wide solid angle EDX detector operated at 200/300kV acceleration voltages [31,32].

The zero-resistance critical temperature, $T_c$, of the films was assessed by d.c. electric measurements in the four-probe configuration. Magnetization measurements were performed using a vibrating sample magnetometer (VSM) equipped with a 12 T magnet and a controlled He gas flow system. Isothermal magnetization loops, $M(H)$ up to 12 T, were recorded at different temperatures. The field swept at a rate of 0.5 T $\text{min}^{-1}$ ($B = \mu_0 H$//YBCO *c*-axis). The critical current density values were extracted from the magnetization data through the Bean model for a rectangular thin film [33].

In order to perform *I-V* transport measurements, the films were patterned, using standard UV photolithography and wet etching to obtain 1 mm long strips with a width of 20 and 50 μm. The patterned samples were mounted on a sample holder and loaded in a He gas flow cryostat provided with a 12 T superconducting magnet. Critical current values as a function of the applied magnetic field were obtained from the *I-V* characteristics using 1 $\mu V \cdot cm^{-1}$ criterion.

## 3. Results and Discussion

### 3.1. Structural Properties and Morphology

Good epitaxial YBCO films were obtained with the addition of both 5% and 10% Gd using both standard and fast-firing conditions. XRD patterns of films obtained with different doping levels are reported in Figure 1. The spectra were characterized by the presence of peaks ascribable to $00\ell$ reflections of the YBCO phase and to the substrate, with few less intense features ascribable to the substrate contribution (e.g., broad halos at $2\theta = 12°$ and 32° and $K_\beta$ reflections) and no clear pieces of evidence of the presence of crystalline secondary phases. Going further into details, from a detailed analysis of the 001 reflections (see inset in the figure), it can be observed that all samples with Gd doping were characterized by the presence of a broad peak at a lower angle with respect to the YBCO reflection. This feature might be ascribed to the presence of $Y_2Ba_4Cu_7O_{15}$ (Y247) phases or $Y_1Ba_2Cu_4O_8$ (Y124) (e.g., PCPDF card # 473–410), suggesting, therefore, a higher amount of stacking faults in these samples. However, this feature was observed only on the 001 reflection, suggesting that the stacking faults were widely dispersed, without the formation of large coherent scattering domains of these phases, and thus limiting the order of observable Bragg reflections.

To evaluate differences in the microstructure due to the chemical composition, the *c* lattice parameter was calculated and is reported in Table 2, as well as the grain size and the microstrain along the *c* axis were evaluated by means of the Williamson–Hall method [35]. It can be observed that all samples were characterized by similar *c* axis values, without a significant effect due to Gd addition. Regarding the grain size, the values were well in agreement with the thickness of the films, suggesting a coherent growth of the YBCO phase from the substrate interface to the film surface. Few differences could be observed also regarding the microstrain values, with results ranging in the 0.05%–0.1% range. Besides, in this case, a clear trend with the doping amount could not be evidenced, suggesting that stress accumulation due to the lattice mismatch between YBCO and GdBCO phases could be relieved through the stacking faults formation.

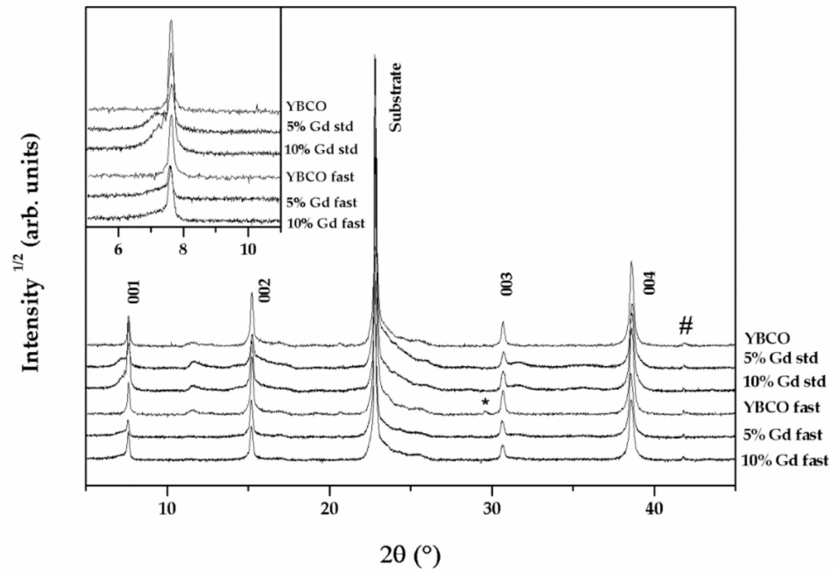

**Figure 1.** X-ray θ-2θ patterns of the different samples deposited by standard (std) and fast process. YBCO $00\ell$ peaks are indicated, while * is ascribable to a Y-Ti-O secondary phase due to the solution-substrate interaction [34]. The symbol # indicates the $K_{\beta}$ peak of the substrate. In the inset: detail of YBCO 001 reflections.

**Table 2.** Results of the XRD analysis for the different samples deposited by the standard and fast process, with lattice parameter $c$, grain size, and microstrain $\varepsilon$ calculated along the $00\ell$ directions:

| Sample | Process | Lattice Parameter $c$ (Å) [1] | Grain Size (nm) | ε (%) |
|---|---|---|---|---|
| YBCO | Standard | 11.67 ± 0.01 | 77 ± 7 | 0.05 ± 0.01 |
| YBCO-Gd 5% | | 11.67 ± 0.01 | 77 ± 3 | 0.07 ± 0.01 |
| YBCO-Gd 10% | | 11.67 ± 0.01 | 70 ± 5 | 0.07 ± 0.01 |
| YBCO | Fast | 11.67 | 100 | 0.08 |
| YBCO-Gd 5% | | 11.68 | 80 | 0.06 |
| YBCO-Gd 10% | | 11.67 | 80 | 0.09 |

[1] For the standard process, the mean and standard deviation of results obtained for several samples prepared in the same laboratory and with the same procedure are provided.

The XPS depth profile of a YBCO-Gd 5% sample grown on an STO substrate is shown in Figure 2. The depth profile consisted of seven sputtering cycles for a 70 min total sputtering time. The interface was reached at about 57 min, resulting in a sputtering rate value of about 1.3 nm·min$^{-1}$. The Gd normalized intensity is shown on the left axis, while the Y, Sr, and Ti intensities are on the right axis. The depth profile showed the Gd intensity increasing with the etched depth, while the Y intensity remained fairly constant up to the interface region. Sr and Ti were also detected all over the thickness, with their intensities increasing in the proximity of the interface region. Diffusion from the STO substrate has been already observed in previous works, and it has been explained as due to the action of the propionic acid used as the solvent [34,36]. Figure 3 shows the Gd/Y distribution along with the −5% sample thickness. The Gd/Y behavior was quite homogeneous in the bulk film, i.e., far from the surface (30 min sputtering time) and up to the interface (57 min sputtering time). The Gd/Y stoichiometric ratio resulted in about 0.06 inside the film and about 0.06 in the total thickness, in good agreement with the nominal Gd 5 mol % content. The stoichiometric behavior of the YBCO-Gd 10% sample resulted similarly to the 5% doped film. In this case, the Gd/Y intensity ratio resulted in about 0.11 in the bulk film and about 0.13 in the total thickness. Figure 4 shows the binding energies of the Gd 3d$_{5/2}$ (Figure 4a) and O1s (Figure 4b), measured on both the 5% and 10% YBCO-Gd samples as a function of the film depth. The binding energy values far from the surface (where they were not influenced by contamination) and before the interface (at about 57 min) were fairly constant. The red dot-dashed lines in Figure 4 indicate the binding energy of the $Gd_2O_3$ sample used as a reference. The corresponding binding energy value measured for the Gd $3d_{5/2}$ and O1s were 1187.0 eV and 530.1 eV, respectively, in agreement with the literature data on $Gd_2O_3$ oxide [37,38].

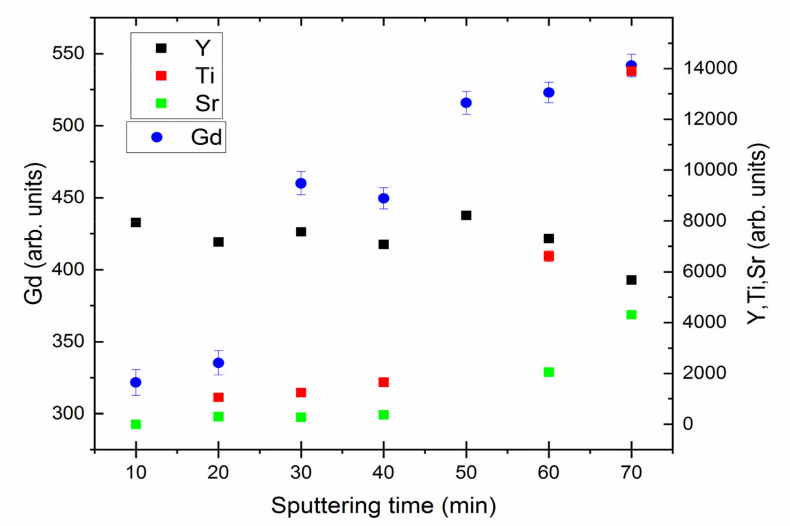

**Figure 2.** Depth profile for YBCO-Gd 5% film deposited by standard process. The error bars are provided for all the elements in the figure.

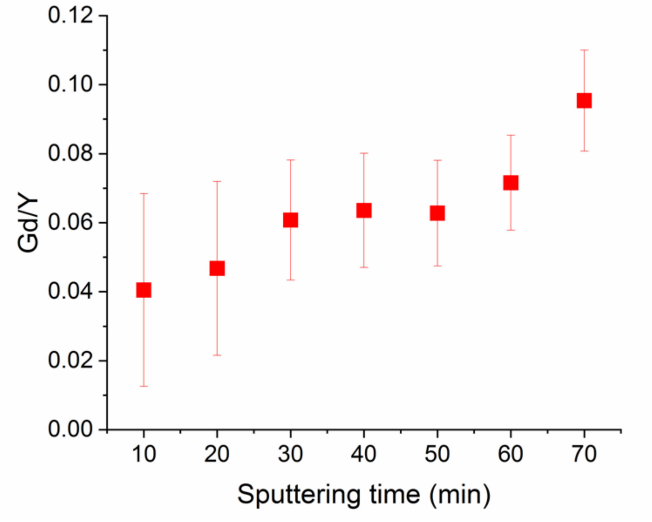

**Figure 3.** Gd/Y stoichiometric ratio was calculated for the YBCO-Gd 5% film deposited by the standard process.

As it can be seen, the position of the O1s and Gd $3d_{5/2}$ in $Gd_2O_3$ were at higher binding energy and well separated from the average binding energy of O1s and Gd $3d_{5/2}$ measured in the YBCO-Gd films. This feature indicated that the electronic environment of Gd in the YBCO-Gd system was not similar to the one of Gd in $Gd_2O_3$. Preliminary results on the GdBCO film suggested that the nature of the Gd bond in YBCO-Gd was closer to Gd in GdBCO [39]. Even though detailed work is still in progress and defined conclusions cannot be drawn, the scenario resulting from XPS investigations was then more consistent with the presence of a GdBCO phase within the YBCO-Gd films rather than Gd oxide formation.

The highly *c*-axis oriented grain structure, revealed by XRD (Figure 1 and Table 2), corresponded to dense, smooth, and well-connected film surfaces observed with SEM (Figure 5). The good morphology of YBCO-Gd films, comparable with those of pure YBCO, evidenced that even 10% of Gd introduction did not produce any film degradation. The YBCO-Gd films obtained by using the fast ramp showed as well a similar morphology with respect to pristine YBCO deposited in the same conditions. As can be seen in Figure 5d–f, some porosity was evident in pure YBCO, but it was almost absent in the Gd-doped films. In general, among YBCO-Gd samples, there were no significant differences due to dopants concentration or ramp rate.

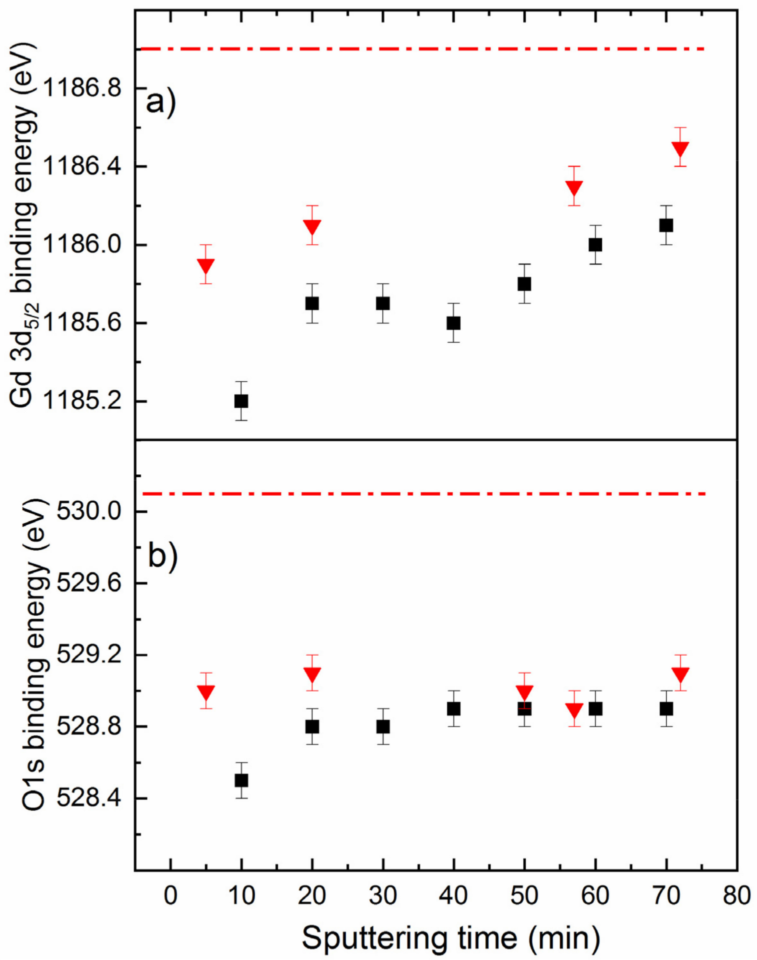

**Figure 4.** Binding energies as a function of the sputtering time for the YBCO-Gd 5% (black squares) and 10% (red triangles) films deposited by standard process. (**a**) Gd $3d_{5/2}$ binding energies; (**b**) O1s binding energies. The red dot-dashed lines indicate the binding energy position of the Gd $3d_{5/2}$ and O1s core-levels measured in $Gd_2O_3$.

Figure 6a shows the HAADF STEM overview of the YBCO-Gd 5% layer on the STO substrate. No precipitate particles or secondary phases ascribable to $RE_2O_3$ were present, in contrast with the previously reported study by [20]. The vertical brighter/darker contrast corresponded to YBCO twin grains with an average size of 18.5 nm in [100]/[010]YBCO projection (giving ~13 nm in [110]YBCO projection).

Figure 6b,c show the presence of Y124 intergrowths (in other words, 'stacking faults') in the YBCO matrix. The edges of these intergrowths produced strain in the YBCO matrix [40]. This strain was visualized by diffraction contrast in ADF STEM images as brighter (Figure 6b) or warmer (Figure 6c) contrast areas. The longer Y124 intergrowths contained Cu/O-deficient areas (see the highlighted area in Figure 6c), which appeared to be 1D ferromagnetic clusters [41]. The visualized features observed in the sample (twins, strains, and clusters in Y124) created a rich pinning landscape.

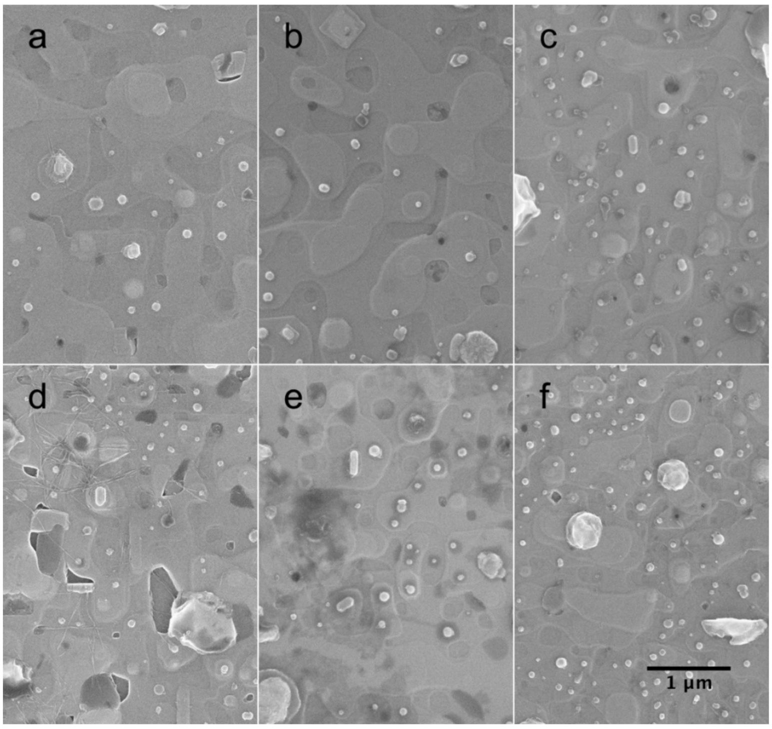

**Figure 5.** SEM images at the same magnification of (**a**) YBCO, (**b**) YBCO-Gd 5%, and (**c**) YBCO-Gd 10% films deposited by the standard process; (**d**) YBCO, (**e**) YBCO-Gd 5%, and (**f**) YBCO-Gd 10% films deposited by the fast process. Scale bar: 1 µm.

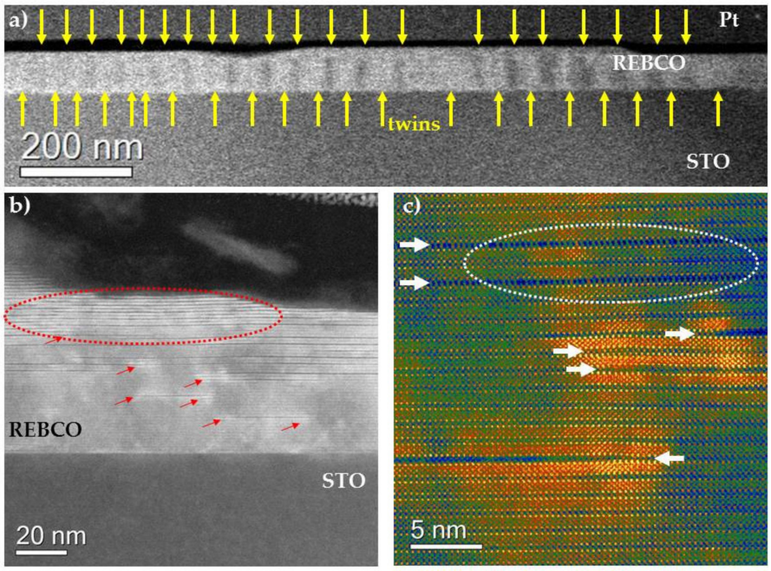

**Figure 6.** (**a**) High-angle annular dark-field scanning transmission electron microscopy (HAADF STEM) overview of YBCO-Gd 5% film deposited by the standard process (taken along the [100]/[010]YBCO zone axis), showing a high density of twins (highlighted by yellow arrows). (**b**) Annular dark-field (ADF) STEM image, demonstrating the presence of Y124 intergrowths. The strained areas of the YBCO matrix around Y124 intergrowths are visible as brighter contrast areas (marked by red arrows and ellipse). (**c**) High-resolution ADF STEM image colored in temperature scale: Y124 intergrowths are marked by white arrows. The edges of these intergrowths produced strained areas in the YBCO matrix (diffraction contrast appeared as warmer contrast areas). The region with a visible concentration of Cu vacancies (ferromagnetic 1D clusters) is highlighted by the white ellipse.

EDX analysis, Figure S1 and Figure 7, confirmed a uniform distribution of Gd in the film being in a good agreement with XPS studies on a larger area (5 mm × 5 mm). Therefore, TEM and XPS results demonstrated that a compositional homogeneity of the YBCO-Gd films was clearly evidenced at different scales. In addition, this analysis showed that the film was perfectly epitaxial to the STO substrate. The integrated profile over the Gd map confirmed that Gd occupied some of the Y positions in YBCO perovskite structure, in agreement with XPS indications.

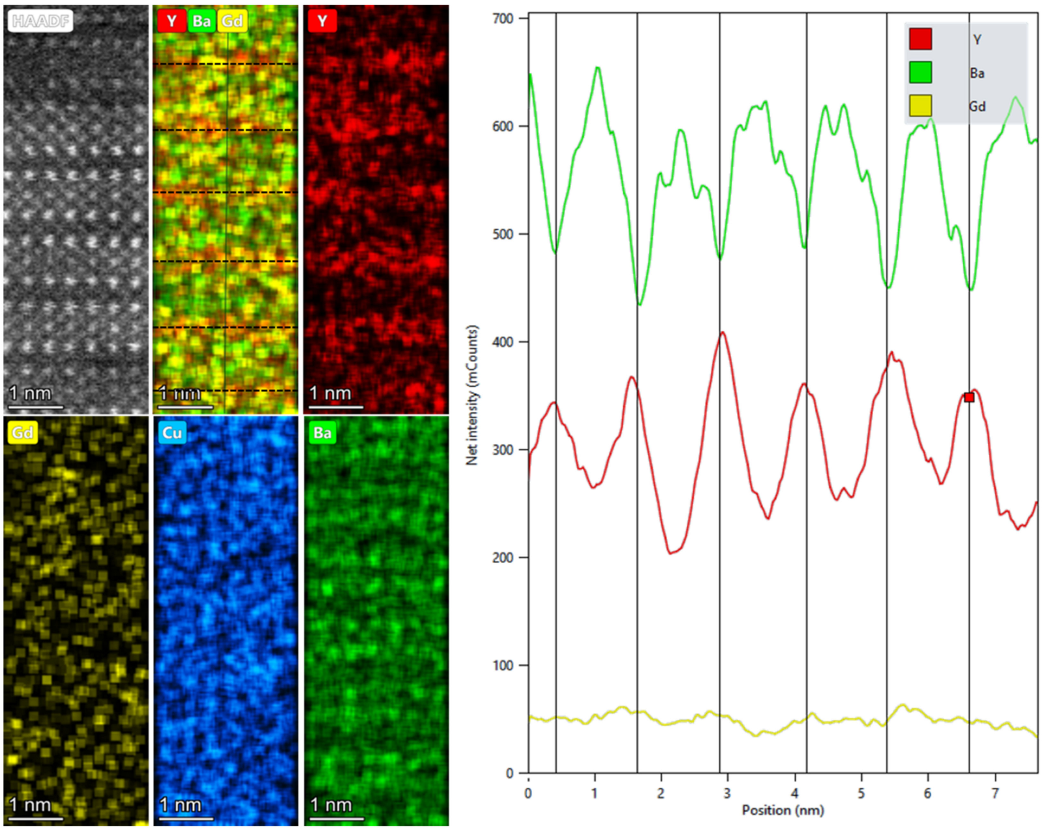

**Figure 7.** High-resolution HAADF STEM together with corresponding elemental Y, Gd, Ba, and Cu EDX maps and the profile over the image (starting from the bottom to the top) of YBCO-Gd 5% film deposited by the standard process. The Y/Gd planes positions are marked by black vertical continuous (profile plot) and horizontal dashed (map image) lines.

Finally, no $RE_2O_3$ was evidenced by XPS or TEM. A limited number of $(Y,Gd)_2Cu_2O_5$ nanoparticles were observed on the surface of the film by TEM. Therefore, we can suppose that the stoichiometric balance could be guaranteed by the presence of other phases like $YGdCu_2O_5$ or $Gd_2BaCuO_5$, being the latter one the GdBCO decomposition product at high $pO_2$ conditions [8]. This point is still not completely elucidated, and it will be studied in more detail.

### 3.2. Superconducting Properties

The $J_c$ behavior by dc measurements of the YBCO-Gd films was investigated in the 10–77 K temperature range as a function of the magnetic field direction and strength. In Figure 8a, the $J_c(H)$ curves of both 5 and 10 mol % Gd samples were plotted. In the same graph, the curves of a typical MOD YBCO films grown in the same process conditions were also shown for a direct comparison. As can be seen, at 77 K, all $J_c$ curves overlapped with some differences only in the mid-field region, approaching the irreversibility field (about 6 T). Reducing the temperature, $J_c$ curves of the YBCO-Gd samples exhibited better in-field behavior than pristine YBCO film in the whole investigated magnetic field region. In Table 3, the $J_c$ values, recorded by magnetic and dc transport measurements, of

YBCO-Gd samples, at selected temperatures and magnetic fields, were compared to the corresponding averaged values of YBCO samples deposited with the standard process conditions. This comparison demonstrated that the improvement induced by Gd addition was a more general and reproducible behavior. Moreover, the $J_c$ values, calculated from VSM magnetization data, were in good agreement with transport data, both at 77 and 65 K, in a broad range of fields. Such positive evidence strengthened the reliability of the following discussion.

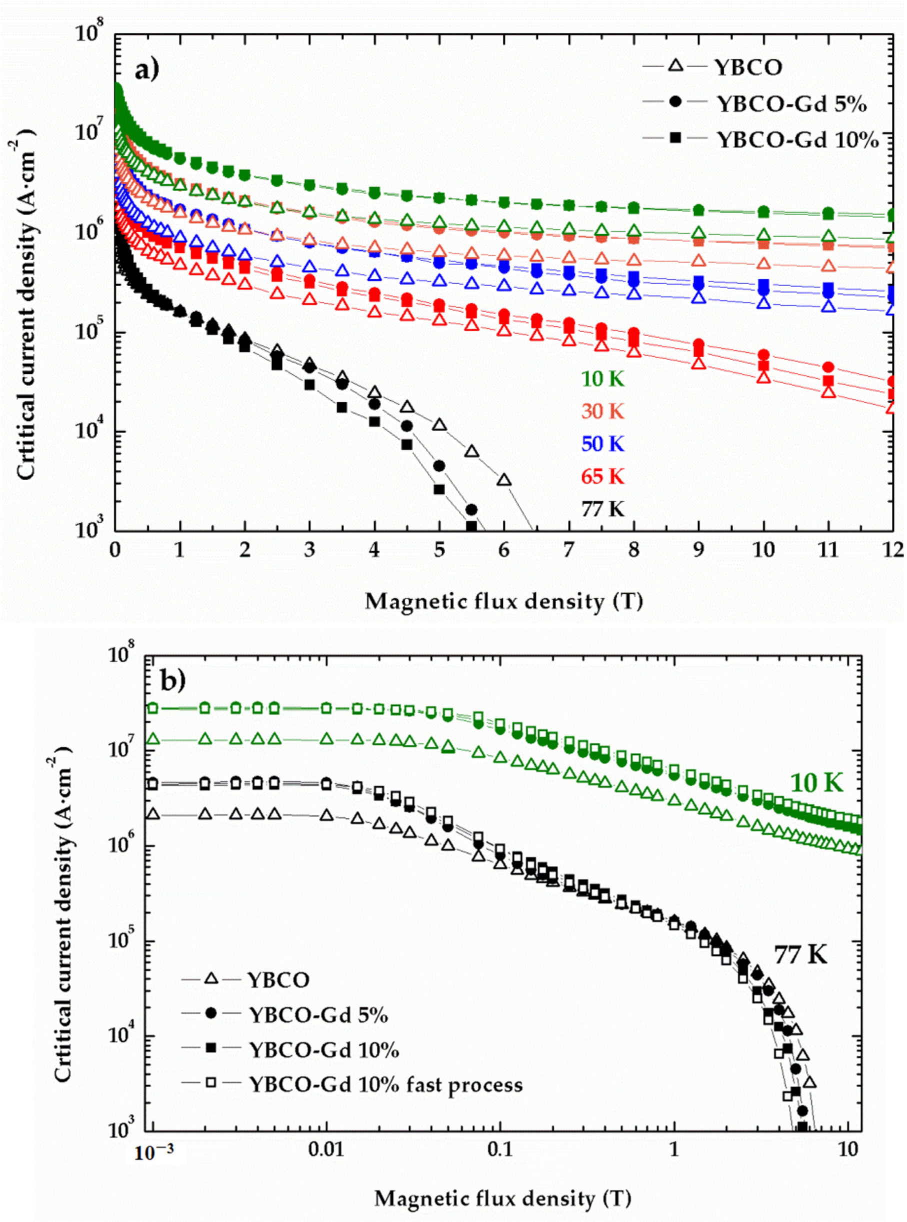

**Figure 8.** (**a**) Transport measurements of critical current density ($J_c$) as a function of the applied magnetic field recorded for pristine YBCO (open triangle), YBCO-Gd 5% (full circle), and YBCO-Gd 10% (full square) films deposited with the standard process at several temperatures (77, 65, 50, 30 and 10 K) with $H//c$-axis condition. In (**b**), the same $J_c(H)$ curves, collected at 77 and 10 K for samples deposited with the standard process, were compared with YBCO-Gd 10% (open square) film grown by the fast process.

**Table 3.** Critical current density ($J_c$) was measured at different temperatures and applied magnetic fields. Magnetic and electric transport analyses were compared[1]. Italics is used for *I-V* data. Films were deposited using the standard process.

| Temperature (K) | Applied Field (T) | $J_c$ | YBCO [2] (MA·cm$^{-2}$) | YBCO-Gd 5% (MA·cm$^{-2}$) | YBCO-Gd 10% (MA·cm$^{-2}$) |
|---|---|---|---|---|---|
| 77 | 0 | VSM | 1.80 ± 0.59 | 3.23 | 2.71 |
| | | *I-V* | *2.26 ± 0.93* | *4.57* | *4.27* |
| | 1 | VSM | 0.10 ± 0.03 | 0.11 | 0.10 |
| | | *I-V* | *0.15 ± 0.04* | *0.16* | *0.16* |
| | 3 | VSM | 0.02 ± 0.01 | 0.03 | 0.01 |
| | | *I-V* | *0.04 ± 0.01* | *0.04* | *0.03* |
| 65 | 0 | VSM | 3.81 ± 1.31 | 6.69 | 6.05 |
| | | *I-V* | *4.37 ± 1.76* | *9.22* | *8.94* |
| | 1 | VSM | 0.40 ± 0.12 | 0.53 | 0.47 |
| | | *I-V* | *0.55 ± 0.15* | *0.77* | *0.70* |
| | 3 | VSM | 0.17 ± 0.05 | 0.23 | 0.21 |
| | | *I-V* | *0.25 ± 0.07* | *0.35* | *0.31* |
| | 9 | VSM | 0.04 ± 0.02 | 0.05 | 0.03 |
| | | *I-V* | *0.08 ± 0.03* | *0.08* | *0.06* |
| 10 | 0 | *I-V* | *13.3 ± 1.2* | *28.4* | *27.2* |
| | 1 | *I-V* | *3.27 ± 0.42* | *5.47* | *5.73* |
| | 3 | *I-V* | *1.91 ± 0.44* | *2.97* | *3.04* |
| | 9 | *I-V* | *1.20 ± 0.32* | *1.70* | *1.65* |

[1] The abbreviation VSM and *I-V* are used for magnetic and electric transport analyses, respectively. [2] YBCO average value represents the mean and standard deviation of results obtained for several YBCO samples prepared in the same laboratory and with the same procedure.

It is worth noticing that a clear trend with the content of Gd excess in YBCO films did not emerge from these measurements. In fact, both Gd 5 and 10 mol % samples exhibited very subtle differences in $J_c$ values and field dependences. This feature could be more consistently evaluated by investigating samples with a higher Gd doping level, and it will be addressed in future works.

Besides the in-field improvement, a remarkable effect of Gd excess was also revealed in self-field $J_c$ values, $J_c(0)$, that were larger than those of YBCO films at all temperatures. In Figure 8b, the $J_c(H)$ curves measured at 77 and 10 K were plotted in a double logarithmic scale, in order to more easily appreciate the low-field region behaviors. In the same Figure 8b, the $J_c(H)$ curves of the YBCO-Gd processed with fast ramp were also reported. As can be seen, the fast ramp process promoted a similar $J_c$ behavior with a slight increase in the low-field region at both temperatures. At high temperature, $J_c(0)$ = 4–5 MA/cm$^2$ was achieved for YBCO-Gd films, corresponding to values more than double with respect to those obtained with the pristine YBCO (see also Table 3 for details). Interestingly, the low-field plateau of $J_c$, representing the field region of a single vortex pinning regime, was not affected by Gd introduction in YBCO films. The cross-over field from single to collective vortex pinning regimes was usually identified by $\mu_0 H^*$, determined at $J_c = 0.9\, J_c(0)$. The calculated values at 77 K were very close to each other to $\mu_0 H^* \approx 15$ mT (Table 4), in line with the typical values reported for MOD YBCO films [42,43]. The similarity in $\mu_0 H^*$ could be explained considering that the introduction of Gd did not significantly alter the nature, i.e., neither the density nor the strength, of the defects acting in the pristine YBCO as vortex pinning centers at high temperatures, such as 77 K. On the other hand, the introduction of Gd promoted a more compact and dense film microstructure, reflected in a better current percolation (increase in $J_c(0)$). The discrepancies at higher magnetic field values indicated, however, that some minor effects were acting in the collective regime.

At lower temperatures, similar features could be recognized in the low-field behavior. At 10 K, the introduction of Gd led to an increase in $J_c(0)$ to about 30 MA·cm$^{-2}$ for both 5 and 10 mol % films (Figure 9a), but, as observed at 77 K, not for $\mu_0 H^*$ (Figure 8b and Table 4). The obtained values in the range 30–50 mT agreed with the reported results for MOD YBCO films at low temperatures. It was observed that the low-temperature value of $\mu_0 H^*$ was directly related to the microstrain generated by the incorporation of nanoparticles in nanocomposite YBCO films. On this basis, the reported $\mu_0 H^*$

values in YBCO-Gd films were consistent with the relatively low effect of Gd addition on the film microstrain (see Table 2) [44].

**Table 4.** Critical temperature ($T_c$), cross over fields ($H^*$), $\alpha$ parameter of the $J_c$ power-law dependence ($J_c(H) = J_c(0) \times H^{-\alpha}$), maximum of the pinning force densities ($F_p^{max}$), and irreversibility field ($H_{irr}$) for YBCO and YBCO-Gd films deposited with the standard process.

| Sample | $T_c$ (K)[1] | $H^*$ (mT) | $\alpha$ | $F_p^{max}$ (GN·m$^{-3}$) | $H^{max}$ (T) | $H_{irr}$ (T) | $H^*$ (mT) | $\alpha$ |
|---|---|---|---|---|---|---|---|---|
| | | | | 77 K | | | 10 K | |
| YBCO | 90.2 ± 0.4 | 17.7 | 0.6 | 2.0 | 1.6 | 6.7 | 39 | 0.5 |
| YBCO-Gd 5% | 90.6 ± 0.2 | 13.7 | 0.6 | 1.8 | 1.5 | 6.5 | 31 | 0.5 |
| YBCO-Gd 10% | 90.3 ± 0.1 | 14.7 | 0.7 | 1.6 | 1.3 | 6.4 | 46 | 0.6 |

[1] The mean and standard deviation of results obtained for several samples prepared with the same procedure are reported.

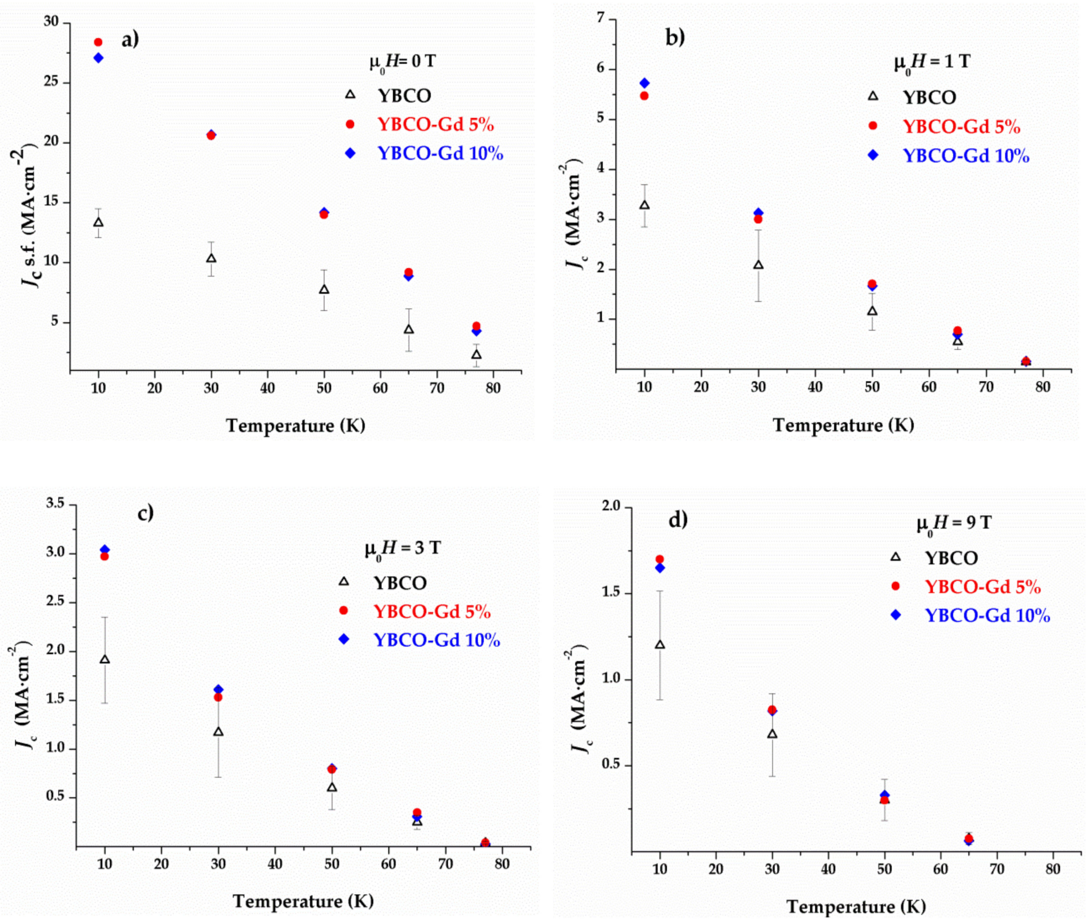

**Figure 9.** Critical current density ($J_c$) in self-field condition (B = 0 T) (**a**), at 1 T (**b**), 3 T (**c**), and 9 T (**d**) measured at different temperatures by dc transport measurements. Error bars of YBCO data were calculated from the standard deviation of results obtained for several YBCO samples prepared in the same laboratory and with the same procedure. Data at 77, 65 and 10 K are also reported in Table 3 (*I-V* data).

On the other hand, the improved in-field values of $J_c$ indicated that a more efficient low-temperature vortex pinning was present in YBCO-Gd films. In Figure 9b–d, the $J_c$ data at different temperatures for selected magnetic fields are reported for a better comparison. As shown by microstructural characterizations, Gd addition promoted a rich defect landscape. Gd was uniformly and finely distributed within the YBCO film matrix, and a large number of stacking faults, i.e., Y124/Y247 phases, was generated. Since this was a typical mechanism of stress release, the presence of stacking faults suggested that during the film growth stage, more stress was accumulated, likely for the accommodation of excess of Gd. As reported by TEM, lattice strain was localized at the edges of stacking faults, acting as efficient pinning centers. Moreover, additional defects recognized within the stacking fault, such as Cu/O vacancies, are proposed as effective pinning centers [41]. In agreement with TEM and XPS results, Gd was expected to be incorporated in YBCO by locally substituting Y in the YBCO crystal structure, thus forming unit cells of the superconducting GdBCO dispersed within the YBCO film matrix. Due to the slight difference in lattice parameters, lattice strain should locally emerge at the interfaces between YBCO and GdBCO phases. Since the local oxygen deficiency is an efficient *c*-axis strain relief mechanism in YBCO films, a strain-induced local oxygen nonstoichiometry could likely emerge in the YBCO lattice close to the YBCO-GdBCO interfaces. This local oxygen nonstoichiometry could produce a point-like vortex pinning center, as already proposed in previous studies on pulsed laser deposited mixed REBCO films [45]. It has to be considered that this kind of defect is particularly efficient in pinning vortices at lower temperature conditions, thus providing an additional isotropic contribution to the increase of the pinning strength at low temperatures.

Angular measurements supported the aforementioned scenario and provided some additional hint on the role of Gd addition on $J_c$ behavior in YBCO films. In Figure 10, the $J_c(\theta)$ angular curves measured at 77 and 30 K and $\mu_0 H = 3$ T for YBCO-Gd and pristine YBCO samples were plotted. At 77 K, the pristine $J_c$ curve exhibited a different dependence with the magnetic field angle. In fact, $J_c$ values were higher than the $J_c$ measured for Gd samples in a wide angular range between about $-45° < \theta < 45°$ (in agreement with the already discussed $J_c(H)$ plotted in Figure 8a), whereas the opposite could be observed in other magnetic field orientations and, in particular, for $\theta = \pm 90°$. These improvements in YBCO-Gd films suggested that *ab*-plane intrinsic pinning was particularly strengthened in such samples. This could be ascribed to the increased density of stacking faults recognized by TEM investigations with respect to the pristine YBCO film. In fact, it is well known that effective *ab*-aligned planar defects often extend their effect on a wider angular range because, due to energetic reasons, it is more convenient for magnetic vortices, within a certain angle spread centered at $\theta = \pm 90°$, to be accommodated along the defect length [46]. More interestingly, it has to be pointed out that in that region, the 10 mol % Gd film had the highest $J_c$ values. $J_c(\theta)$ curves recorded at both 77 and 30 K for YBCO-Gd 10 mol % with faster temperature ramp appeared very similar to the standard ramp sample, indicating that the increase from 10 to 30 °C·min$^{-1}$ was not enough to promote significant changes in YBCO-Gd films, in agreement with previous analyses.

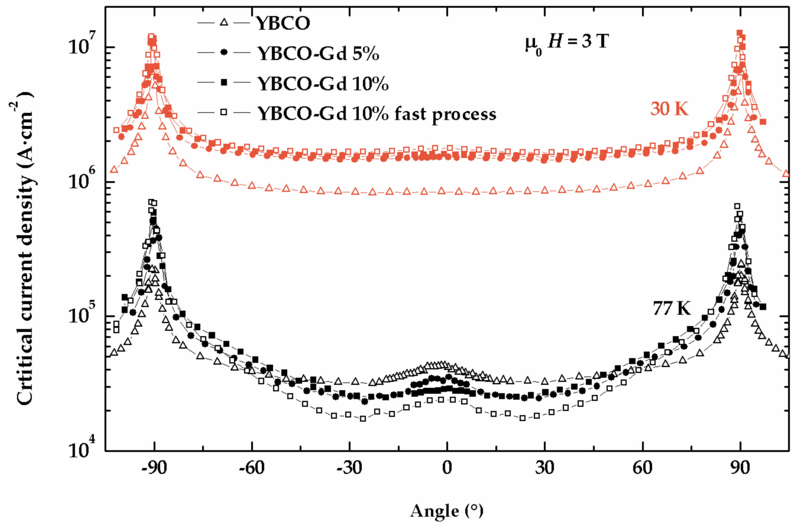

**Figure 10.** Angular dependence of $J_c$ at 77 and 30 K and applied field value of 3 T recorded for pristine YBCO (open triangle), YBCO-Gd 5% (full circle), and YBCO-Gd 10% (full square) films deposited with the standard process and YBCO-Gd 10% (open square) film deposited with the fast process. Zero degrees correspond to the field orientation, parallel to the YBCO *c*-axis.

Looking at the $J_c(\theta)$ curves at 30 K, since similar *ab*-plane peak broadening was observed, it was inferred that this mechanism was less effective at low temperature, likely due to the increased stiffness of vortex lines at lower temperatures. In addition, the $J_c(\theta)$ curves measured at 30 K revealed a very similar dependence between Gd-added and pristine YBCO films, with YBCO-Gd samples having $J_c$ values higher in the whole angular range. The observed behavior indicated that defects related to Gd addition had an isotropic character and strengthened their pinning capability as the temperature was reduced. These features were consistent with the proposed local strain accumulation at GdBCO/YBCO interfaces.

The broad bump centered at $\theta = 0^\circ$ in the $J_c(\theta)$ could be attributed to the twin boundary pinning contribution, which resulted particularly effective when these boundaries, extending over the entire film thickness (see Figure 6a), acted as directional pinning centers, as often recognized in MOD YBCO samples. At 30 K, the broad bump was weakened, as often reported for the twin boundary pinning contribution [47].

It is now worth drawing some remarks, even taking into account the results reported by previous work on a similar system, i.e., the addition of 10 mol % Gd to YBCO film by the sol-gel method [20]. Li et al. observed an increase in both $T_c$ and $J_c$ in the whole field range at 77 K. These authors ascribed the enhancement to the significant presence of $RE_2O_3$ phases in their films. In our work, instead, we observed a different behavior: $T_c$ was not affected by Gd addition (Table 4), whereas $J_c$ behaviors were more markedly improved at lower temperatures rather than at 77 K. This result, in agreement with the structural and morphological characterizations, evidenced the effect of the different nature of the introduced defects (no $RE_2O_3$ phases were recognized in our samples), likely due to the different growth methods [20].

In this sense, the improvement of $J_c$ observed in the present study was consistent with what was reported in the literature, relatively to Y replacement by Gd in YBCO-GdBCO systems deposited by MOD [6,16]. Actually, the present XPS and TEM investigations suggested that also in our samples, Y substitution by Gd occurred despite the unfavorable conditions for GdBCO nucleation ($pO_2$ too high and thermal treatment ramp rates too slow for GdBCO film [8,9]). The findings of our work were in agreement with previous results obtained by Hayashi et al. on (Y,Pr)BCO films [48]. The authors of that work assumed that both YBCO and PrBCO formed, although PrBCO nucleation requires a $pO_2$ at least 1000 times lower than that necessary for YBCO formation. This inconsistency can be explained considering that since the YBCO growth temperature is lower than GdBCO one, the YBCO lattice starts to nucleate first and then acts as a suitable template for the successive GdBCO nucleation. This feature deserves more attention, and more detailed studies are in progress based on thermodynamic and kinetic approaches [49].

## 4. Conclusions

Highly epitaxial Gd-doped YBCO films were deposited through the process optimized for pure YBCO. A uniform Gd distribution, revealed by both XPS and TEM, corresponded to improved superconducting properties with respect to pristine YBCO. It seemed to be confirmed that the presence of different defects, originated from Y and Gd competition during REBCO phase formation, had a beneficial effect on transport properties, particularly significant at low temperatures. These results suggested that homogeneously dispersed nano-sized defects could be originated even by an in situ YBCO with Gd excess approach, avoiding the complex use of nanoparticles required by the ex-situ route.

Further investigations will focus on the tuning of Gd and Y phase formation through experimental condition optimization. Higher dopant concentrations will be also evaluated.

**Supplementary Materials:** The following are available online at http://www.mdpi.com/2079-6412/10/9/860/s1, Figure S1: TEM overview of YBCO-Gd 5% film deposited with the standard process. Cross-section view: HAADF STEM image, showing the mapped area together with elemental Y, Gd, Ba, and Cu EDX maps, confirming a uniform Y and Gd distribution. (a) HAADF STEM overview of YBCO-Gd 5% film deposited by the standard process YBCO layer morphology. The $(Gd,Y)_2Cu_2O_5$ precipitate is highlighted by a yellow circle. The area of EDX mapping is shown by the red rectangle. (b) Elemental Gd, Pt, Y, Si, Cu, O, Ba, Ti, and Sr EDX maps confirm a uniform Y and Gd distribution. (c) EDX spectrum from the YBCO layer area proves Gd presence in the layer.

**Author Contributions:** Conceptualization, V.P. and G.C.; methodology, V.P. and G.C.; formal analysis, V.P., G.C., A.V., A.A.A., F.R., A.M. (Andrea Masi), and A.S.; investigation, V.P., A.V., A.A.A., F.R., A.S., A.M. (Alexander Meledin), and F.M.F.; resources, V.P., A.V., A.A.A., F.R., A.S., A.M. (Alexander Meledin), and G.C.; writing—Original draft preparation, V.P., G.C., A.M. (Andrea Masi), and A.S.; writing—Review and editing, V.P., G.C., A.V., A.A.A., F.R., A.S., A.M. (Alexander Meledin), and S.O.; visualization, V.P., G.C., A.M. (Andrea Masi), A.S., A.M. (Alexander Meledin), and A.V.; supervision, G.C. and S.O.; project administration, G.C.; funding acquisition, G.C. All authors have read and agreed to the published version of the manuscript.

**Funding:** This work has been carried out within the framework of the EUROfusion Consortium and has received funding from the Euratom program 2014–2018 and 2019–2020 under grant agreement No 633053. The views and opinions expressed herein do not necessarily reflect those of the European Commission. TEM analysis was funded from the European Union's Horizon 2020 research and innovation program under grant agreement No.823717—ESTEEM3 (Nano-engineered YBCO Superconducting Tapes for High Field Applications, NESTApp).

**Acknowledgments:** V.P.'s work has been carried out within the framework of the XXXIII Doctoral program in Chemical Sciences, Department of Chemical Science and Technologies, University of Rome Tor Vergata.

**Conflicts of Interest:** The authors declare no conflict of interest. The funders had no role in the design of the study; in the collection, analyses, or interpretation of data; in the writing of the manuscript, or in the decision to publish the results.

## References

1. Erbe, M.; Cayado, P.; Freitag, W.; Ackermann, K.; Langer, M.; Meledin, A.; Hänisch, J.; Holzapfel, B. Comparative study of CSD-grown *RE*BCO films with different rare earth elements: Processing windows and $T_c$. *Supercond. Sci. Technol.* **2020**. [CrossRef]
2. Lao, M.; Willa, R.; Meledin, A.; Rijckaert, H.; Chepikov, V.; Lee, S.; Petrykin, V.; Driessche, I.V.; Molodyk, A.; Holzapfel, B.; et al. In-field performance and flux pinning mechanism of pulsed laser deposition grown $BaSnO_3$/$GdBa_2Cu_3O_{7-\$}$\updelta$ nanocomposite coated conductors by SuperOx. *Supercond. Sci. Technol.* **2019**, *32*, 094003. [CrossRef]
3. Wang, Y.; Xu, D.; Li, Y.; Liu, L. Dependencies of microstructure and stress on the thickness of $GdBa_2Cu_3O_7$ $-\delta$ thin films fabricated by RF sputtering. *Nanoscale Res. Lett.* **2013**, *8*, 304. [CrossRef] [PubMed]
4. Oh, W.-J.; Park, I.; Lee, J.-H.; Lee, H.; Moon, S.-H.; Shinde, K.; Chung, K.; Yoo, S.-I. The post-annealing effect on the pinning properties of $GdBa_2Cu_3O_{7-\delta}$ coated conductors via RCE-DR. *IEEE Trans. Appl. Supercond.* **2018**, *28*, 1–5. [CrossRef]
5. Cayado, P.; Mundet, B.; Eloussifi, H.; Vallés, F.; Coll, M.; Ricart, S.; Gázquez, J.; Palau, A.; Roura, P.; Farjas, J.; et al. Epitaxial superconducting $GdBa_2Cu_3O_{7-\delta}$/$Gd_2O_3$ nanocomposite thin films from advanced low-fluorine solutions. *Supercond. Sci. Technol.* **2017**, *30*, 125010. [CrossRef]
6. Erbe, M.; Hänisch, J.; Hühne, R.; Freudenberg, T.; Kirchner, A.; Molina-Luna, L.; Damm, C.; Van Tendeloo, G.; Kaskel, S.; Schultz, L.; et al. $BaHfO_3$ artificial pinning centres in TFA-MOD-derived YBCO and GdBCO thin films. *Supercond. Sci. Technol.* **2015**, *28*, 114002. [CrossRef]
7. Pop, C.; Villarejo, B.; Pino, F.; Mundet, B.; Ricart, S.; de Palau, M.; Puig, T.; Obradors, X. Growth of all-chemical high critical current $YBa_2Cu_3O_{7-\$}$\updelta$ thick films and coated conductors. *Supercond. Sci. Technol.* **2018**, *32*, 015004. [CrossRef]
8. Lee, J.-W.; Choi, S.-M.; Song, J.-H.; Lee, J.-H.; Moon, S.-H.; Yoo, S.-I. Stability phase diagram of $GdBa_2Cu_3O_{7-\delta}$ in low oxygen pressures. *J. Alloy. Compd.* **2014**, *602*, 78–86. [CrossRef]
9. Iguchi, T.; Araki, T.; Yamada, Y.; Hirabayashi, I.; Ikuta, H. Fabrication of Gd Ba Cu O films by the metal organic deposition method using trifluoroacetates. *Supercond. Sci. Technol.* **2002**, *15*, 1415–1420. [CrossRef]
10. Cayado, P.; Erbe, M.; Kauffmann-Weiss, S.; Bühler, C.; Jung, A.; Hänisch, J.; Holzapfel, B. Large critical current densities and pinning forces in CSD-grown superconducting $GdBa_2Cu_3O_{7-x}$-$BaHfO_3$ nanocomposite films. *Supercond. Sci. Technol.* **2017**, *30*, 094007. [CrossRef]
11. Sun, M.J.; Liu, W.Q.; He, K.; Liu, Z.Y.; Chen, S.G.; Cai, C.B. Orientation behavior and mechanism of Ag-doped $GdBa_2Cu_3O_{7-\delta}$ superconducting thin films derived by metal organic deposition. *J. Supercond. Nov. Magn.* **2018**, *31*, 3159–3162. [CrossRef]

12. Xu, A.; Delgado, L.; Khatri, N.; Liu, Y.; Selvamanickam, V.; Abraimov, D.; Jaroszynski, J.; Kametani, F.; Larbalestier, D.C. Strongly enhanced vortex pinning from 4 to 77 K in magnetic fields up to 31 T in 15 mol.% Zr-added (Gd, Y)-Ba-Cu-O superconducting tapes. *APL Mater.* **2014**, *2*, 046111. [CrossRef]
13. Miura, M.; Kato, T.; Yoshizumi, M.; Yamada, Y.; Izumi, T.; Hirayama, T.; Shiohara, Y. Rare earth substitution effects and magnetic field dependence of critical current in $Y_{1-x}RE_xBa_2Cu_3O_y$ coated conductors with nanoparticles (RE=Sm, Gd). *Appl. Phys. Express* **2009**, *2*, 023002. [CrossRef]
14. Nakaoka, K.; Yoshida, R.; Sato, M.; Ibi, A.; Machi, T.; Izumi, T. Optimization of interim heat-treatment condition on TFA-MOD process for fabrication of $Y_{0.77}Gd_{0.23}Ba_2Cu_3O_y$ coated conductors with $BaHfO_3$. *J. Phys. Conf. Ser.* **2019**, *1293*, 012035. [CrossRef]
15. Dong, Z.; Ding, F.; Zhang, H.; Shang, H.; Huang, D.; Xu, W.; Li, T.; Zou, Q.; Gu, H. Preparation of high performance YGdBCO films by low fluorine TFA-MOD process. *J. Rare Earths* **2020**, *38*, 755–762. [CrossRef]
16. Jian, H.; Shao, D.; Yang, Z.; Zhu, X.; Sun, Y. Jc enhancement and flux pinning in $Y_{1-x}Gd_xBCO$ and (Gd, Eu) codoped $Y_{0.9-y}Eu_yGd_{0.1}BCO$ thin films by TFA-MOD. *Phys. C Supercond.* **2013**, *488*, 39–45. [CrossRef]
17. Miura, M.; Maiorov, B.; Baily, S.A.; Haberkorn, N.; Willis, J.O.; Marken, K.; Izumi, T.; Shiohara, Y.; Civale, L. Mixed pinning landscape in nanoparticle-introduced $YGdBa_2Cu_3O_y$ films grown by metal organic deposition. *Phys. Rev. B* **2011**, *83*, 184519. [CrossRef]
18. Cayado, P.; Erbe, M.; Kauffmann-Weiss, S.; Jung, A.; Hänisch, J.; Holzapfel, B. Chemical solution deposition of $Y_{1-x}Gd_xBa_2Cu_3O_{7-\delta}$–$BaHfO_3$ nanocomposite films: Combined influence of nanoparticles and rare-earth mixing on growth conditions and transport properties. *RSC Adv.* **2018**, *8*, 42398–42404. [CrossRef]
19. Xu, S.; Wu, X.S.; Ma, G.B.; Wang, Z.H.; Gao, J. Effects of $Gd_2O_3$ addition in $YBa_2Cu_3O_{7-\delta}$ on the critical current density. *J. Appl. Phys.* **2008**, *103*, 07C714. [CrossRef]
20. Li, C.S.; Jin, L.H.; Yu, Z.M.; Zhang, S.N.; Lu, Y.F.; Feng, J.Q.; Wang, Y.; Zhang, P.X. Enhanced flux pinning in YGdBCO film grown by sol–gel approach. *J. Sol-Gel Sci. Technol.* **2014**, *70*, 67–71. [CrossRef]
21. Cayado, P. Multifunctional Nanostructured Superconductors by Chemical Routes: Towards High Current Conductors. Ph.D. Thesis, Barcelona Autonomous University, Barcelona, Spain, 2016.
22. Obradors, X.; Puig, T.; Li, Z.; Pop, C.; Mundet, B.; Chamorro, N.; Vallés, F.; Coll, M.; Ricart, S.; Vallejo, B.; et al. Epitaxial $YBa_2Cu_3O_{7-x}$ nanocomposite films and coated conductors from Ba $MO_3$ ($M$ = Zr, Hf) colloidal solutions. *Supercond. Sci. Technol.* **2018**, *31*, 044001. [CrossRef]
23. De Keukeleere, K.; Cayado, P.; Meledin, A.; Vallès, F.; De Roo, J.; Rijckaert, H.; Pollefeyt, G.; Bruneel, E.; Palau, A.; Coll, M.; et al. Superconducting $YBa_2Cu_3O_{7-\delta}$ nanocomposites using preformed $ZrO_2$ nanocrystals: Growth mechanisms and vortex pinning properties. *Adv. Electron. Mater.* **2016**, *2*, 1600161. [CrossRef]
24. Coll, M.; Guzman, R.; Garcés, P.; Gazquez, J.; Rouco, V.; Palau, A.; Ye, S.; Magen, C.; Suo, H.; Castro, H.; et al. Size-controlled spontaneously segregated $Ba_2YTaO_6$ nanoparticles in $YBa_2Cu_3O_7$ nanocomposites obtained by chemical solution deposition. *Supercond. Sci. Technol.* **2014**, *27*, 044008. [CrossRef]
25. Prado, F.; Caneiro, A.; Serquis, A. High temperature thermodynamic properties, orthorhombic/tetragonal transition and phase stability of $GdBa_2Cu_3O_y$ and related R123 compounds. *Phys. C Supercond. Appl.* **1998**, *295*, 235–246. [CrossRef]
26. Adachi, G.; Imanaka, N. The Binary Rare Earth Oxides. *Chem. Rev.* **1998**, *98*, 1479–1514. [CrossRef] [PubMed]
27. Eyring, L. Chapter 27 The binary rare earth oxides. In *Handbook on the Physics and Chemistry of Rare Earths*; Elsevier: Amsterdam, The Netherlands, 1979; Volume 3, pp. 337–399. ISBN 978-0-444-85215-1.
28. Meledin, A.; Turner, S.; Cayado, P.; Mundet, B.; Solano, E.; Ricart, S.; Ros, J.; Puig, T.; Obradors, X.; Van Tendeloo, G. Unique nanostructural features in Fe, Mn-doped YBCO thin films. *Supercond. Sci. Technol.* **2016**, *29*, 125009. [CrossRef]
29. Pinto, V.; Lamanna, R.; Vannozzi, A.; Angrisani Armenio, A.; De Marzi, G.; Augieri, A.; Piperno, L.; Sotgiu, G.; Celentano, G. Solution Refining for MOD-YBCO Optimization: An NMR Study. *IEEE Trans. Appl. Supercond.* **2018**, *28*, 1–5. [CrossRef]
30. Anthony, M.T. Spectrometer calibration. In *Practical Surface Analysis by Auger and X-ray Photoelectron Spectroscopy*; Briggs, D., Seah, M.P., Eds.; John Wiley and Sons: Hoboken, NJ, USA, 1983; pp. 429–435.
31. Kovács, A.; Schierholz, R.; Tillmann, K. FEI Titan G2 80-200 CREWLEY. *J. Large-Scale Res. Facil. JLSRF* **2016**, *2*, 43. [CrossRef]
32. Heggen, M.; Luysberg, M.; Tillmann, K. FEI Titan 80-300 STEM. *J. Large-Scale Res. Facil. JLSRF* **2016**, *2*, 42. [CrossRef]
33. Bean, C.P. Magnetization of High-Field Superconductors. *Rev. Mod. Phys.* **1964**, *36*, 31–39. [CrossRef]

34. Santoni, A.; Rondino, F.; Piperno, L.; Armenio Angrisani, A.; Pinto, V.; Mancini, A.; Augieri, A.; Frolova, A.; Rufoloni, A.; Vannozzi, A.; et al. Zirconium distribution in solution-derived $BaZrO_3$-$\gamma Ba_2Cu_3O_{7-\delta}$ epitaxial thin films studied by X-ray photoelectron spectroscopy. *Thin Solid Films* **2019**, *669*, 531–536. [CrossRef]
35. Mote, V.; Purushotham, Y.; Dole, B. Williamson-Hall analysis in estimation of lattice strain in nanometer-sized ZnO particles. *J. Theor. Appl. Phys.* **2012**, *6*, 2–9. [CrossRef]
36. Piperno, L.; Vannozzi, A.; Pinto, V.; Angrisani Armenio, A.; Rondino, F.; Santoni, A.; Mancini, A.; Rufoloni, A.; Augieri, A.; Tortora, L.; et al. Interaction between untreated $SrTiO_3$ substrates and solution-derived $YBa_2Cu_3O_{7\text{-}\delta}$ films. *Appl. Surf. Sci.* **2020**, *528*, 146402. [CrossRef]
37. Barreca, D.; Gasparotto, A.; Milanov, A.; Tondello, E.; Devi, A.; Fischer, R.A. $Gd_2O_3$ Nanostructured Thin Films Analyzed by XPS. *Surf. Sci. Spectra* **2007**, *14*, 60–67. [CrossRef]
38. Jeon, S.; Hwang, H. Effect of hygroscopic nature on the electrical characteristics of lanthanide oxides ($Pr_2O_3$, $Sm_2O_3$, $Gd_2O_3$, and $Dy_2O_3$). *J. Appl. Phys.* **2003**, *93*, 6393–6395. [CrossRef]
39. Santoni, A.; Pinto, V.; Masi, A.; Cayado, P.; Celentano, G. Gd nanoinclusions in epitaxial YBCO thin films studied by X-ray Photoelectron Spectroscopy. 2020; in press.
40. Guzman, R.; Gazquez, J.; Mundet, B.; Coll, M.; Obradors, X.; Puig, T. Probing localized strain in solution-derived $YBa_2Cu_3O_{7-\delta}$ nanocomposite thin films. *Phys. Rev. Mater.* **2017**, *1*, 024801. [CrossRef]
41. Gazquez, J.; Guzman, R.; Mishra, R.; Bartolomé, E.; Salafranca, J.; Magén, C.; Varela, M.; Coll, M.; Palau, A.; Valvidares, S.M.; et al. Emerging Diluted Ferromagnetism in High-Tc Superconductors Driven by Point Defect Clusters. *Adv. Sci.* **2016**, *3*, 1500295. [CrossRef]
42. Palau, A.; Vallès, F.; Rouco, V.; Coll, M.; Li, Z.; Pop, C.; Mundet, B.; Gàzquez, J.; Guzman, R.; Gutierrez, J.; et al. Disentangling vortex pinning landscape in chemical solution deposited superconducting $YBa_2Cu_3O_{7-x}$ films and nanocomposites. *Supercond. Sci. Technol.* **2018**, *31*, 034004. [CrossRef]
43. Bartolomé, E.; Alcalà, J.; Vallès, F.; Puig, T.; Obradors, X.; Pompeo, N.; Alimenti, A.; Torokhtii, K.; Rizzo, F.; Augieri, A.; et al. Vortex pinning properties at dc and microwave frequencies of $YBa_2Cu_3O_{7-x}$ films with nanorods and nanoparticles. *Supercond. Sci. Technol.* **2020**, *33*, 074006. [CrossRef]
44. Li, Z.; Coll, M.; Mundet, B.; Chamorro, N.; Vallès, F.; Palau, A.; Gazquez, J.; Ricart, S.; Puig, T.; Obradors, X. Control of nanostructure and pinning properties in solution deposited $YBa_2Cu_3O_{7-x}$ nanocomposites with preformed perovskite nanoparticles. *Sci. Rep.* **2019**, *9*, 5828. [CrossRef]
45. MacManus-Driscoll, J.L.; Foltyn, S.R.; Jia, Q.X.; Wang, H.; Serquis, A.; Maiorov, B.; Civale, L.; Lin, Y.; Hawley, M.E.; Maley, M.P.; et al. Systematic enhancement of in-field critical current density with rare-earth ion size variance in superconducting rare-earth barium cuprate films. *Appl. Phys. Lett.* **2004**, *84*, 5329–5331. [CrossRef]
46. Civale, L.; Maiorov, B.; Serquis, A.; Willis, J.O.; Coulter, J.Y.; Wang, H.; Jia, Q.X.; Arendt, P.N.; MacManus-Driscoll, J.L.; Maley, M.P.; et al. Angular-dependent vortex pinning mechanisms in $YBa_2Cu_3O_7$ coated conductors and thin films. *Appl. Phys. Lett.* **2004**, *84*, 2121–2123. [CrossRef]
47. Rouco, V.; Palau, A.; Guzman, R.; Gazquez, J.; Coll, M.; Obradors, X.; Puig, T. Role of twin boundaries on vortex pinning of CSD YBCO nanocomposites. *Supercond. Sci. Technol.* **2014**, *27*, 125009. [CrossRef]
48. Hayashi, M.; Araki, T.; Ishii, H.; Nishijima, G.; Matsumoto, A. Atom-replaced pins in a Y-based superconductor—Single-crystalline perovskite structure including both $PrBa_2Cu_3O_{7-x}$ and $YBa_2Cu_3O_{7-y}$. *Supercond. Sci. Technol.* **2018**, *31*, 055013. [CrossRef]
49. Pinto, V.; Celentano, G.; Tomellini, M. Heterogeneous nucleation of YBCO via fluorine based MOD process: thermodynamic and kinetic approach. *Supercond. Sci. Technol.* **2020**, *33*, 115006. [CrossRef]